Journal of Alloys and Compounds 492 (2010) 128–133

Contents lists available at ScienceDirect

Journal of Alloys and Compounds

journal homepage: www.elsevier.com/locate/jallcom

Al–($L1_2$)Al_3Ti nanocomposites prepared by mechanical alloying: Synthesis and mechanical properties

S.S. Nayak[a,*], S.K. Pabi[a], B.S. Murty[b]

[a] Department of Metallurgical and Materials Engineering, Indian Institute of Technology Kharagpur, West Bengal 721 302, India
[b] Department of Metallurgical and Materials Engineering, Indian Institute of Technology Madras, Chennai 600 036, India

ARTICLE INFO

Article history:
Received 25 June 2009
Received in revised form 28 October 2009
Accepted 29 October 2009
Available online 24 November 2009

Keywords:
Mechanical alloying and milling
Trialuminides
Nanocomposites
Dispersion strengthening

ABSTRACT

The present paper reports the formation of nanocomposites containing α-Al and $L1_2$–Al_3Ti in binary Al–Ti alloys containing 5, 10, 15, and 20 at.% Ti. Supersaturated solid solution of Ti in Al was observed after 20 h of mechanical alloying irrespective of the Ti content. Nanocomposites formed after mechanical alloying and subsequent annealing at 673 K for 2 h showed a high hardness (3.4 GPa), modulus (106.4 GPa) and density (95%). Hardness values of Al–($L1_2$)Al_3Ti nanocomposites obtained by nanoindentation were similar to hardness measured with microhardness. High strength of the nanocomposites was attributed to the formation of large volume fraction of nanocrystalline $L1_2$–Al_3Ti particles and the ultrafine grain size of α-Al matrix.

1. Introduction

Many of the currently available Al alloys do not exhibit satisfactory results at high temperature [1] and have a useful upper limit of 598 K. The reason being the dispersoids present in Al alloys coarsen too fast at this temperature and thus the strength and creep resistance are likely to degrade. In conventionally processed metal matrix composites (MMCs), by powder metallurgy route, the reinforcing particles are formed prior to their addition to the matrix metal [2] and the scale of reinforcing phase is limited by the starting powder size, which is typically of the order of several to tens of micrometers and rarely below 1 μm. It is widely recognized that the mechanical properties of MMCs are controlled, to a large extent, by the size and volume fraction of the reinforcements, as well as, the nature of the matrix–reinforcement interface [2]. Superior mechanical properties can be achieved when fine and stable reinforcements with good interfacial bonding are dispersed uniformly in the matrix. A possible alternative is to form the reinforcement *in situ* in the metal matrix [3]. The advantages of *in situ* MMCs are that they have more homogeneous microstructure and are thermodynamically more stable. Moreover, they also have strong interfacial bonding between the reinforcements and the matrices. *In situ* aluminum matrix composites may be fabricated by various techniques, such as conventional ingot metallurgy, mechanical alloying (MA), rapid solidification processing (RSP), and combustion synthesis. However, materials produced by MA, RSP or combustion synthesis must be densified, by a hot consolidation process such as hot isostatic pressing/extrusion [4–6] or spark plasma sintering [7–9], in order to obtain the final product.

Aluminum alloys reinforced with trialuminide particles (Al_3Ni, Al_3Fe, Al_3Ti, Al_3Zr, etc.) possess high specific strength, high specific modulus, and excellent properties both at ambient and elevated temperatures [10–12]. In comparison to most other aluminum-rich intermetallics, Al_3Ti is very attractive because it has higher melting point (~1623 K) and relatively low density (3.4 g/cm^3). Further, Ti has low diffusivity and solubility in aluminum and hence Al_3Ti is expected to exhibit a low coarsening rate at elevated temperature [13]. In addition, the Young's modulus of Al_3Ti phase is reported to be 216 GPa [14]. Therefore, the presence of Al_3Ti phase is very effective in increasing the stiffness of aluminum alloys. Al–Al_3Ti nanocomposites have been fabricated by RSP [12,15,16] and MA [17,18] to achieve high strength. The major strengthening mechanisms, which contribute to the high strength of Al–Al_3Ti alloys, have been suggested to include Orowan strengthening, grain size strengthening, and load-shearing effects of Al_3Ti particles [12,19,20].

The objective of the present work was to produce fully dense Al-based nanocomposites, with different volume fractions of nanometer-sized metastable $L1_2$–Al_3Ti intermetallic as reinforcement particle, by MA. The basic idea of fabricating the Al-based nanocomposites by MA lies in examining the stability of the metastable $L1_2$–Al_3Ti phase so as to maintain the Ni-based

* Corresponding author. Present address: Centre for Advanced Materials Joining, University of Waterloo, Canada. Tel.: +1 519 888 4567x35256; fax: +1 519 885 5862.
E-mail addresses: sashank@uwaterloo.ca, sashank.nayak@gmail.com (S.S. Nayak).

0925-8388/$ – see front matter © 2009 Elsevier B.V. All rights reserved.
doi:10.1016/j.jallcom.2009.10.274

Table 1
Compositions and conditions of MA used in the present study for the synthesis of Al-based nanocomposites.

Systems	Compositions studied	Milling conditions
Al–Ti	$Al_{100-x}Ti_x$ for x = 5, 10, 15 and 20	Mill: Planetary Fritsch P5 Vials and balls: Tungsten carbide Milling speed: 300 rpm Milling medium: Toluene Milling time: 20 h Diameter of balls: 10 mm BPR = 10:1

superalloy like microstructure both at room temperature, as well as, at elevated temperatures. Also, MA was adopted for the synthesis of nanocomposites because, (a) being a far-from-equilibrium process provides ample scope for easy formation of metastable phase like $L1_2$ structure [21–24], (b) involves severe plastic deformation to promote uniform mixing and refining of the constituent phases in the all materials, and (c) easy consolidation and subsequent annealing for good densification, as reported recently by the present authors [23,24].

2. Experimental details

Table 1 illustrates the conditions of MA used and the compositions studied in the present work. Raw materials used for MA were high purity elements *viz.* Al (99.9 wt.%) and Ti (99.7 wt.%). Al powder was of particle size less than 45 μm (−325 mesh) and Ti was used in the form of sponge. To avoid oxidation of powders toluene was used to fill the vials up to a level to just cover the balls and powders. The cold compaction of MA powders was carried out using a load of 375 MPa into pellets of 12 mm diameter. The cold compacted pellets were sintered at 573 K and 673 K for 2 h under a flowing argon atmosphere. In addition, mechanically alloyed Al–Ti alloy powders were hot pressed at 673 K using a load of 490 MPa into a cylindrical shape of 20 mm diameter. Density of green compacts, annealed compacts and hot pressed samples was calculated using simple Archimedes' principle.

Mechanically alloyed samples and cold-consolidated pellets were characterized by Phillips PW 1710 X-Ray Diffractometer using Co-K_α radiation, whereas phase analysis of annealed samples was done using PHILIPS X'Pert PRO using Cu-K_α radiation. Crystallite size of mechanically alloyed powder particles was determined form the X-ray peak broadening by the peak profile analysis using Viogt's single peak method [25] after eliminating the instrumental broadening. Grain coarsening and phase transformation, if any, also were analyzed using X-ray diffraction (XRD). Microhardness was measured under a load of 300 g with a dwelling time of 15 s using a LECO DM-400 hardness tester. An average of at least 10 measurements was taken for each microhardness value. Nanoindentation on pellets of Al–Ti alloys was carried out for the measurement of hardness and elastic modulus in a MTS Nano Indenter® XP using a diamond Berkovich indenter with equilateral triangular faces.

3. Results and discussion

3.1. MA of Al–Ti alloys

Fig. 1a shows the XRD patterns of Al–5Ti[1] alloy after different duration of MA. Peaks of Ti were not observed within 5 h of MA suggesting the formation of Al(Ti) supersaturated solid solution (SSSS) that was stable even after prolonged MA, *i.e.* for 20 h. Close observation of the XRD patterns showed a continuous broadening of XRD peaks with duration of MA, indicating refinement of powder crystallites. The crystallite size measured using (1 1 1) peak profile of Al was 81 nm after 5 h of MA (Fig. 1b). The crystallites got refined further with prolonged MA and the size reached a value of 23 nm after 20 h of MA (Fig. 1b). A gradual decrease in crystallite size from 81 nm (after 5 h of MA) to a final size of 23 nm (after 20 h MA) can be seen from the plot of crystallite size and duration of MA (Fig. 1b). Apart from peak broadening, a small shift in the peak position towards the higher diffraction angle was observed (Fig. 1a)

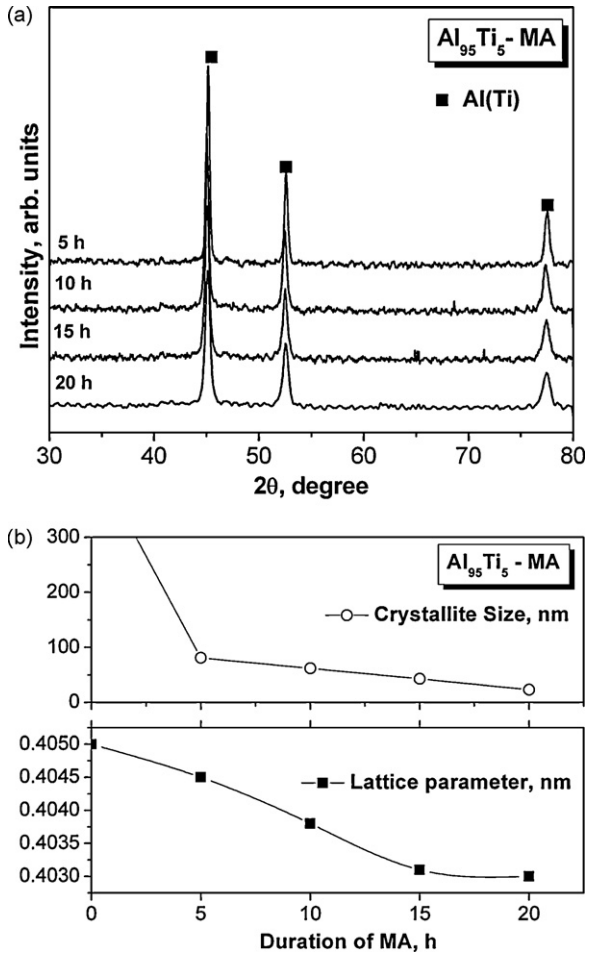

Fig. 1. (a) XRD patterns of $Al_{95}Ti_5$ alloy after 5, 10, 15 and 20 h of MA and (b) variation of lattice parameter and crystallite size of $Al_{95}Ti_5$ alloy with duration of MA.

indicating a decrease in the lattice parameter of the Al as illustrated in Fig. 1b. This suggests incorporation of Ti into the Al lattice. Formation of metastable or stable intermetallics such as Al_3Ti was not observed in Al–5Ti blend up to 20 h of MA. So, it may be concluded that all of Ti are in the form of SSSS.

Similar to Al–5Ti blend, rest of the compositions also showed evidence of formation of SSSS of Ti in Al after 20 h of MA (Fig. 2a). In order to elucidate this aspect, variation of lattice parameter of Al with duration of MA in all the alloys is plotted in Fig. 2b. From the difference in lattice parameter [26] of the Al after 0 h and 20 h of MA in the Al–Ti alloys studied, it can be inferred that 2–3% Ti has dissolved in Al (Table 2). This value is higher than that previously reported by MA [27]. Kim et al. [27] have reported Ti solubility of 2.4 wt.% (1.37%) in Al–20 wt.% Ti (12.3%Ti) alloy. Furthermore, as there was no indication of formation of any new phase after 20 h of MA, it may be concluded that all Ti are in the SSSS formed during MA. In addition to dissolution of Ti into Al, there was evidence of refinement of the crystallites, as indicated by the peak broadening in XRD (Fig. 2a). A continuous decrease

Table 2
Lattice parameter, Ti solubility (as calculated from the change in lattice parameter of Al) and crystallite size of Al–Ti alloys after 20 h of MA.

Composition	Lattice parameter, nm	Solubility, %	Crystallite size, nm
Al–5Ti	0.4030	2.0	23
Al–10Ti	0.4027	2.3	21
Al–15Ti	0.4026	2.4	20
Al–20Ti	0.4020	3.0	19

[1] All compositions reported in this work are in atomic percentage, unless otherwise specified.

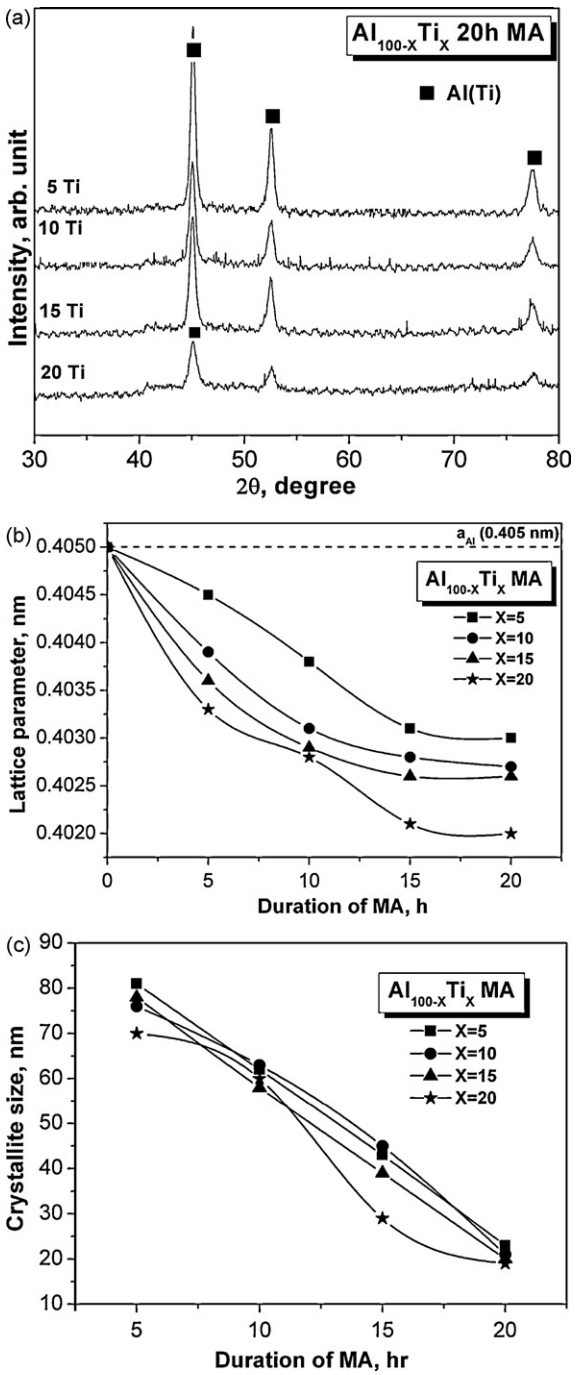

Fig. 2. (a) XRD patterns of $Al_{100-x}Ti_x$ (for $x = 5$, 10, 15 and 20) after 20 h of MA and variation of (b) lattice parameter and (c) crystallite size of Al in $Al_{100-x}Ti_x$ alloys after different durations of MA.

in crystallite size with duration of MA was observed irrespective of the composition studied (Fig. 2c). The final crystallite size of all the alloys was in the range of 19–23 nm after 20 h of MA (Table 2).

3.2. Annealing of nanocrystalline Al–Ti alloys

As MA resulted only in formation of SSSS of Ti in Al, annealing of the nanocrystalline solid solution powder was expected to precipitate out the probable Al_3Ti intermetallic to form the nanocomposites. To know the temperature of precipitation of Al_3Ti intermetallic, DSC of the 20 h MA powders was carried out at a heating rate of 40 K/min. DSC trace of Al–5Ti alloy is shown in Fig. 3, which depicts an exotherm in the temperature range 623–723 K with the peak maximum at 683 K signifying expected precipitation of Al_3Ti intermetallic phase. Along with the exotherm an endotherm at 933 K is evident (Fig. 3), which corresponds to the melting of the Al matrix. It may be noted that all other compositions have also shown similar DSC traces with the exotherm shifting to lower temperature with increasing Ti content in the alloy.

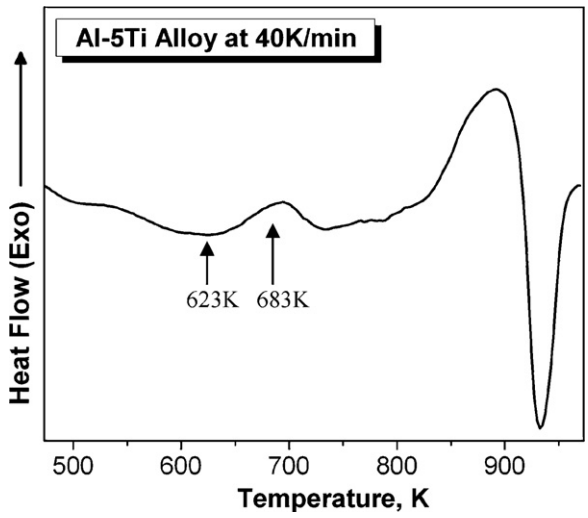

Fig. 3. DSC thermogram of Al–5Ti alloy powder obtained after 20 h MA.

Based on the DSC results, annealing of the 20 h MA powders of all compositions was carried out at two different temperatures 573 K and 673 K for 2 h. The XRD patterns of all Al–Ti alloys after annealing for 2 h at 573 K and 673 K are illustrated in Fig. 4a and b, respectively. Annealing at 573 K has resulted in the commencement of the precipitation of $L1_2$–Al_3Ti intermetallic in all the alloys, including the Al–5Ti alloy that showed an exotherm at 683 K. Precipitation of Al_3Ti is evident from the XRD patterns of all alloys (Fig. 4a), which show a shoulder on (1 1 1) peak of Al. Interestingly, (1 1 0) superlattice reflection of $L1_2$–Al_3Ti phase was also observed, as marked by S(1 1 0) in the XRD patterns (Fig. 4). It may be noted here that the no superlattice reflection of $L1_2$–Al_3Ti was observed in the as-milled condition in binary $Al_{75}Ti_{25}$ composition in our earlier work [21–24]. The (1 1 0) superlattice reflection observed in this study is attributed to annihilation of the defects which were introduced into the alloy powders during MA and the peak sharpening due to grain coarsening, both due to annealing. Fig. 4 also shows that the α-Al peak intensity decreases while that of $L1_2$–Al_3Ti increases with increase in Ti content in the alloy, which is indicative of increase in the volume fraction of the latter. Indication of the formation of DO_{22}–Al_3Ti along with $L1_2$–Al_3Ti phase is also seen (Fig. 4). The intensity of DO_{22} peak is higher in the Al–Ti alloys annealed at 673 K (Fig. 4b), indicating partial transformation of $L1_2$ structure to DO_{22}. The results obtained from XRD analyses of Al–Ti alloys after annealing at 673 K for 2 h are given in Table 3. Crystallite sizes of all the phases formed after annealing show a decreasing value with increase in Ti content in the alloys, evidencing formation of high volume fraction of the $L1_2$–Al_3Ti, that restricts the growth of the α-Al. LRO of $L1_2$–Al_3Ti intermetallic, calculated using the equation reported earlier by the present authors [24], was also found to decrease with increase in Ti content. It may be noted that in TiC peak was observed in samples annealed at low temperature of 573 K (Fig. 4a) but it was barely observed in high temperature (673 K) annealed Al–Ti alloys (Fig. 4b).

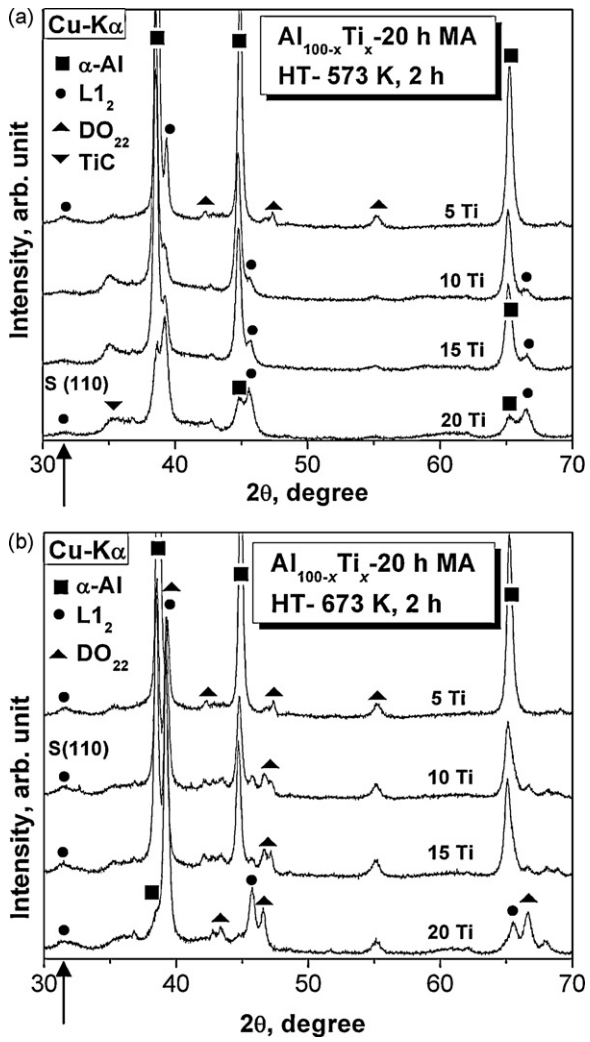

Fig. 4. XRD patterns of the $Al_{100-x}Ti_x$ alloys after annealing for 2 h at (a) 573 K and (b) 673 K.

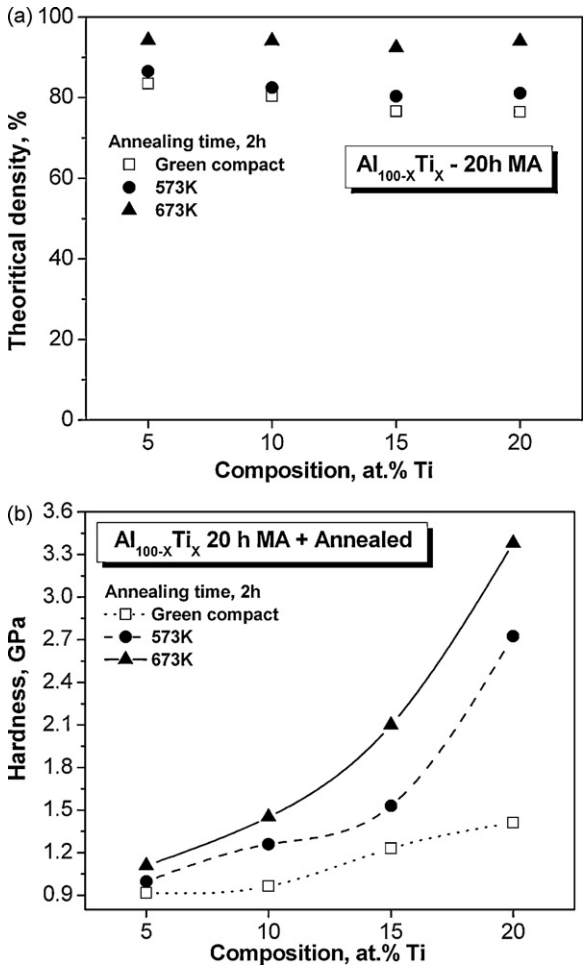

Fig. 5. Variation of (a) density and (b) microhardness of the consolidated nanocrystalline Al–Ti alloy powders before and after annealing at 573 K and 673 K.

3.3. Mechanical properties of nanocomposites prepared by MA

In accordance to the results of XRD studies of MA powders and annealed alloys mentioned in previous sections, the structure of annealed Al–Ti alloy powders consist nanocrystalline Al_3Ti intermetallic particles (both $L1_2$ and DO_{22} structure) dispersed in an ultrafine α-Al matrix forming nanocomposites. To evaluate the mechanical properties of these nanocomposites, nanocrystalline powders obtained after 20 h of MA were consolidated and their hardness was measured. Variation of density and microhardness of the nanocomposites are plotted as a function of Ti content in the alloys as shown in Fig. 5a and b, respectively.

Table 3
Phase evolution after annealing at 673 K for 2 h, crystallite size of the α-Al matrix and LRO (S) of $L1_2$–Al_3Ti phase in various Al–Ti alloys.

Composition	Phase formation after annealing at 673 K for 2 h (crystallite size, nm)	LRO (S)[a]
Al–5Ti	α-Al (80) + $L1_2$–Al_3Ti (45) + DO_{22}–Al_3Ti (62)	0.61
Al–10Ti	α-Al (72) + $L1_2$–Al_3Ti (38) + DO_{22}–Al_3Ti (54)	0.49
Al–15Ti	α-Al (66) + $L1_2$–Al_3Ti (25) + DO_{22}–Al_3Ti (50)	0.39
Al–20Ti	$L1_2$–Al_3Ti (55) + DO_{22}–Al_3Ti + negligible vol.% of α-Al	0.16

[a] LRO was calculated using the equation reported in an earlier work [24].

The measured density of the nanocomposite pellets annealed at 673 K for 2 h was found to be close to 95% of its theoretical value, irrespective of the alloy composition. It may be noted that the theoretical density was calculated presuming that the nanocomposites consist of only Al and Al_3Ti phases, and that the alloy compositions studied are in atomic percent. It may be mentioned here that slight TiC formation was observed only in the alloys annealed at 573 K and not at 673 K and was not considered in density calculation. However, the green compacts and the pellets annealed at lower temperature did not result in a density comparable to high temperature annealed pellets and were found to be in the range of 75–85%. Hardness values of the green compacts containing only nanocrystalline Al(Ti) super saturated solid solution, was found in the range 0.9–1.4 GPa (Fig. 5b). However, annealing at 573 K and 673 K, which resulted in formation of Al–($L1_2$)Al_3Ti nanocomposites, increases the hardness of Al–Ti alloys significantly except for the Al–5Ti alloy (Fig. 5b). The lower hardness of annealed Al–5Ti alloy could be attributed to very small volume fraction of Al_3Ti precipitates.

Nanoindentation study was carried out on all consolidated pellets mentioned above to confirm the microhardness results. Fig. 6a shows the nanohardness variation with depth into the surface of the Al–20Ti pellets, indicating an increase in nanohardness from green compacts to those annealed at 673 K, supporting the microhardness results (Fig. 5b). Hardness and modulus measured by nanoindentation of Al–Ti nanocomposites after annealing at 673 K for 2 h is plotted as a function of volume fraction of Al_3Ti (Fig. 6b). The volume fraction was calculated assuming that all the Ti added

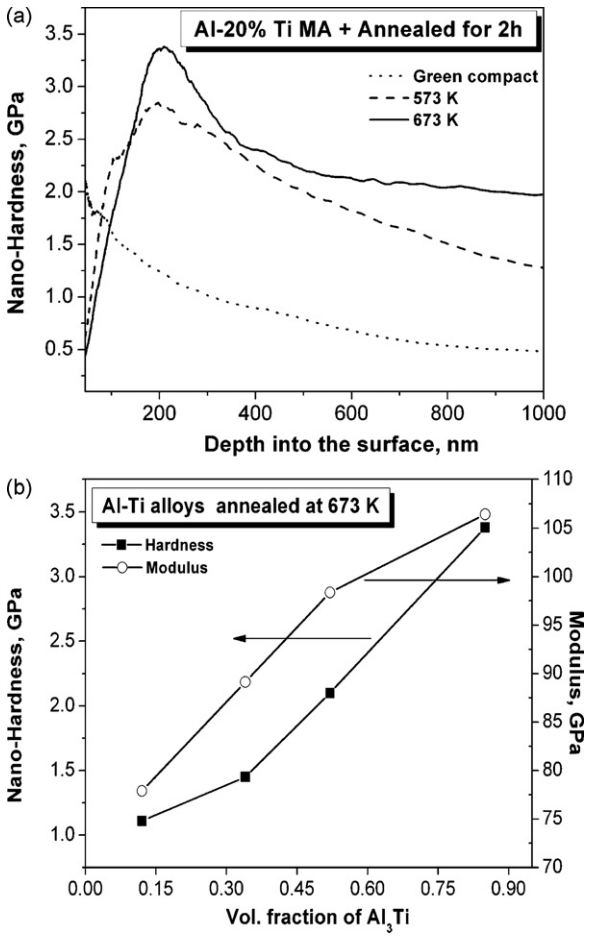

Fig. 6. (a) Nanoindentation results of Al–20Ti alloy powder after green compaction and after sintering the compacts for 2 h at 573 and 673 K; (b) variation of hardness and modulus measured by nanoindentation as a function of volume fraction of Al_3Ti in the nanocomposites after annealing at 673 K for 2 h.

reacted with Al to form Al_3Ti intermetallic. The results of density, volume fraction of Al_3Ti particles and mechanical properties of nanocomposite prepared after MA followed by annealing at 673 K for 2 h in each alloy are listed in Table 4.

The hardness and modulus values shown in Table 4 are measured using nanoindentation. Both nanohardness as well as modulus increase significantly with increasing volume fraction of Al_3Ti. For nanocomposites in Al–20Ti alloy, the nanohardness and Young's modulus was measured to be 3.4 GPa and 106.4 GPa, respectively. Because of the high elastic modulus of Al_3Ti (216 GPa), the Young's modulus of the Al–Al_3Ti nanocomposites increases significantly with increasing the volume fraction of Al_3Ti (Fig. 6b). The Young's modulus of particle-reinforced composites can be predicted from the Halpin–Tsai equation as reported recently by Hsu et al. [28];

$$E_c = \frac{E_m(1+\eta q V)}{E_p(1-qV)}$$

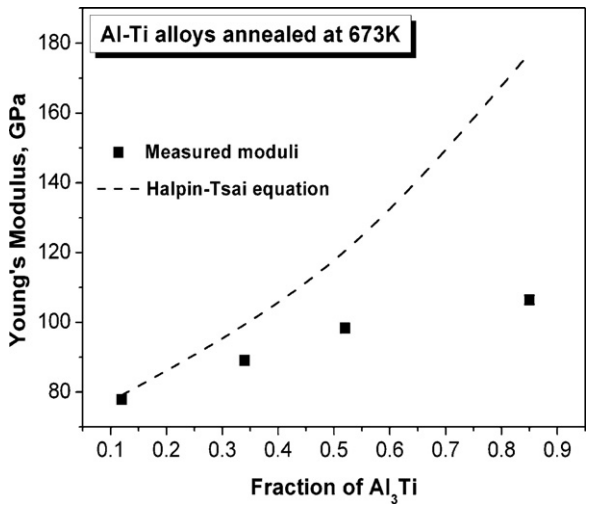

Fig. 7. Variation of Young's modulus of Al–Al_3Ti nanocomposites as a function of volume fraction of Al_3Ti. The prediction using the Halpin–Tsai equation is shown by the dashed line.

where E_c, E_m, and E_p are the Young's moduli of the composite, matrix, and particle, respectively, q is an adjustable parameter, and V is the volume fraction of the particles. For Al–Al_3Ti composites, E_m = 70 GPa and E_p = 216 GPa [8]. By taking η = 1, the calculated Young's moduli of Al–Al_3Ti composites were compared with the measured modulus of nanocomposites in the present work by plotting the same as a function of the volume fraction of Al_3Ti particles (Fig. 7).

At lower volume fraction measured modulus matches exactly with that predicted by Halpin–Tsai equation as shown in Fig. 7. However, the measured Young's moduli of Al–Al_3Ti nanocomposites diverts more and more from the prediction of the Halpin–Tsai equation with the increase in volume fraction of Al_3Ti. This suggests that there is good bonding between Al_3Ti particles and the Al matrix at lower volume fraction of Al_3Ti particle in the nanocomposites so that Al_3Ti particles can contribute effectively to load sharing in the composites. But higher volume fraction of Al_3Ti makes the bonding weaker and hence may not result in effective load sharing and may lead to weak strength of the nanocomposites [28].

Generally, the analysis of the strengthening mechanisms in particulate reinforced alloys is quite difficult because the microstructure of the matrix is inevitably affected by the size, shape, and amount of the reinforcement particles. According to Table 4, the only distinct microstructural variable within the alloy series is the Al_3Ti content. The present alloys may be considered as fine Al–Al_3Ti two-phase composites with ultrafine-grained aluminum matrix. The possible strengthening mechanisms which may operate in particle-reinforced metal matrix composites [29] and hence in the nanocomposites prepared in the present work are manifold and hence the yield strength is assumed to be a summation of the many contributions *viz.* (a) solid solution strengthening, (b) precipitate strengthening, (c) grain and substructure strengthening, and (d) work hardening, due to the strain misfit between the elastic reinforcing particles and the plastic matrix.

Table 4
Density, volume fraction of Al_3Ti and mechanical properties of Al–$L1_2$–Al_3Ti nanocomposites prepared in Al–Ti alloys by MA and annealing at 673 K for 2 h.

Alloy	Theoretical density, %	Calculated % of Al_3Ti	Modulus (E), GPa	Hardness (H_v), GPa	Empirical σ_y, MPa[a]
Al–5Ti	94.3	0.12	77. 9	1.1	370
Al–10Ti	94.1	0.34	89.1	1.5	483
Al–15Ti	92.4	0.52	98.4	2.1	700
Al–20Ti	94.0	0.85	106.4	3.4	1126

[a] $\sigma_y = H_v/3$.

Table 5
Calculated contributions of grain size strengthening (σ_{gs}) and precipitate strengthening (σ_{prec}) to the empirical yield strength of Al–Al_3Ti nanocomposites prepared after annealing at 673 K for 2 h.

Alloy	σ_{gs}, MPa	σ_{prec}, MPa	$\sigma_{gs}+\sigma_{prec}$, MPa	Empirical σ_y, MPa
Al–5Ti	274.6	65.5	340.1	370
Al–10Ti	288.8	232.3	521.1	483
Al–15Ti	315.1	715.7	1030.8	700
Al–20Ti	–	–	–	1126

In the present work, solid solution strengthening can be negligible as it is considered that all the solute has precipitated out giving Al_3Ti intermetallic after annealing. Based on the crystallite size measured from XRD peak profile (Table 3) and the typical microstructure of Al–Al_3Ti nanocomposites [20,28], the major contributions to the strength of nanocomposites reported in the present work are (1) the fine grain size of Al matrix and (2) precipitate strengthening due to fine Al_3Ti particles. The total yield strength of the nanocomposites therefore reduces to the sum of these two terms, $\sigma_y = \sigma_{gs} + \sigma_{prec}$. The contribution to strength from the fine grain size can be calculated from the Hall–Petch equation, $\sigma_{gs} = \sigma_o + kd^{-1/2}$, where σ_o refers to the inherent friction stress of the material, k is a constant referring to an increase in strength caused by grain boundaries and d denotes the size of the Al matrix grains. σ_o = 13 MPa and k = 74 MPa $\mu m^{1/2}$ for pure Al [30].

To estimate the contribution of precipitate strengthening by the $L1_2$–Al_3Ti particles, it is assumed that the Al_3Ti particles are spherical and uniformly distributed. The value of σ_{prec} corresponds to the flow stress contribution due to resistance to dislocation motion, originating from the dispersed intermetallic particles. $\sigma_{prec} = 2Gb/\lambda$, where G and b refer to the shear modulus of the matrix and Burger's vector of the dislocation. For pure Al, these values are taken to be 26 GPa and 0.286 nm, respectively, λ referring to the interparticle spacing of the dispersed Al_3Ti particles can be calculated using the equation below [28],

$$\lambda = \left[\left(\sqrt{\frac{\pi}{V}}\right) - 2\right]\left(\sqrt{\frac{2}{3}}\right) r$$

where r is the radius of the Al_3Ti particle and refers to half of the crystallite size, assuming the particles are spherical, measured from XRD peak profile (Table 3). Based upon the microstructural parameters listed in Table 3, the contributions of grain size strengthening and precipitate strengthening to empirical yield strength (Table 4) were calculated and shown in Table 5. For Al–20%Ti alloy, the contributions of grain refinement and precipitate strengthening could not be calculated due to the difficulty in measuring the grain size of Al from XRD pattern (Fig. 4) and also the formation of very high volume fraction (0.85) of Al_3Ti particle in it after annealing at 673 K (Table 4). Hence it is concluded that the high strength and modulus of Al–$L1_2$(Al_3Ti) nanocomposites can be attributed to the presence of large volume fraction of nanocrystalline $L1_2$–Al_3Ti particles as well as the ultrafine grain size of α-Al matrix. One possible reason for the deviation of the calculated from the measured empirical values could be the assumptions made in the calculation, such as the use of grain sizes measured from the XRD patterns. In addition, it is not clear whether the empirical constant relating the hardness and yield strength changes in case of nanocrystalline materials.

4. Summary

Formation of nanostructured supersaturated solid solution was observed in all the Al–Ti alloys after 20 h of MA. Nanocomposites with $L1_2$–Al_3Ti have been successfully synthesized in Al–Ti alloys with high hardness of 3.4 GPa and modulus of 106.4 GPa by annealing the mechanically alloyed powders. The high strength of Al–$L1_2$(Al_3Ti) nanocomposites was attributed to the presence of large volume fraction of nanocrystalline $L1_2$–Al_3Ti particles and the ultrafine grain size of the Al matrix.

Acknowledgements

S.S. Nayak acknowledges the financial support provided by Council of Scientific and Industrial Research (CSIR), New Delhi to carry out this work. The present work is also partly sponsored by the Department of Science and Technology (grant no. SR/S5/NM-S1/2002).

References

[1] M.E. Fine, Metall. Trans. A 6 (1975) 625.
[2] T.W. Clyne, P.J. Withers, An Introduction to Metal Matrix Composites, Cambridge University Press, Cambridge, 1993.
[3] S.C. Tjong, Z.Y. Ma, Mater. Sci. Eng. R 29 (2000) 49.
[4] C. Goujon, P. Goeuriot, Mater. Sci. Eng. A 356 (2003) 399.
[5] D.B. Witkin, E.J. Laverni, Prog. Mater. Sci. 51 (2006) 1.
[6] H.B. Yu, D.L. Zhang, Y.Y. Chen, P. Cao, B. Gabbitas, J. Alloys Compd. 474 (2009) 105.
[7] T.T. Sasaki, T. Ohkubo, K. Hono, Acta Mater. 57 (2009) 3529.
[8] D. Roy, S. Kumari, R. Mitra, I. Manna, Intermetallics 15 (2007) 1595.
[9] C.K. Kim, S. Lee, S.Y. Shin, D.H. Kim, J. Alloys Compd. 453 (2008) 108.
[10] S. Srinivasan, S.R. Chen, R.B. Schwarz, Mater. Sci. Eng. A 153 (1992) 691.
[11] R.A. Varin, Metall. Mater. Trans. A 33 (2002) 193.
[12] J.M. Wu, S.L. Zheng, Z.Z. Li, Mater. Sci. Eng. A 289 (2000) 246.
[13] S.K. Das, L.A. Davis, Mater. Sci. Eng. A 98 (1988) 1.
[14] M. Nakamura, K. Kimura, J. Mater. Sci. 26 (1991) 2208.
[15] X.C. Tong, H.S. Fang, Metall. Mater. Trans. A 29 (1998) 893.
[16] S.S. Nayak, S.K. Pabi, D.H. Kim, B.S. Murty, Intermetallics (2009), doi:10.1016/j.intermet.2009.09.009.
[17] R. Lerf, D.G. Morris, Mater. Sci. Eng. A 128 (1990) 119.
[18] S.H. Wang, P.W. Kao, Acta Mater. 46 (1998) 2675.
[19] C.F. Feng, L. Froyen, Acta Mater. 47 (1999) 4571.
[20] S.H. Wang, P.W. Kao, C.P. Chang, Scripta Mater. 40 (1999) 289.
[21] S.S. Nayak, B.S. Murty, Trans. Ind. Inst. Met. 46 (2003) 457.
[22] S.S. Nayak, B.S. Murty, Mater. Sci. Eng. A 367 (2004) 218.
[23] S.S. Nayak, D.H. Kim, S.K. Pabi, B.S. Murty, Trans. Ind. Inst. Met. 59 (2006) 193.
[24] S.S. Nayak, S.K. Pabi, B.S. Murty, Intermetallics 15 (2007) 26.
[25] T.H. de Keijser, J.I. Langford, E.I. Mittemeijer, A.B.P. Vogels, J. Appl. Crystallogr. 15 (1982) 308.
[26] W.B. Pearson, A Hand Book of Lattice Spacings and Structures of Metals and Alloys, Pergamon, Oxford, 1974.
[27] G.H. Kim, S.H. Kim, Dong-Wha Kum, Scripta Mater. 34 (1996) 421.
[28] C.J. Hsu, C.Y. Chang, P.W. Kao, N.J. Ho, C.P. Chang, Acta Mater. 54 (2006) 5241.
[29] D.J. Lloyd, Int. Mater. Rev. 39 (1994) 1.
[30] C.Y. Yu, P.W. Kao, C.P. Chang, Acta Mater. 53 (2005) 4019.